

ROTORCRAFT AEROMECHANICS APPLICATIONS OF A COMPREHENSIVE ANALYSIS

Wayne Johnson

*Johnson Aeronautics
Palo Alto, California*

Results from the comprehensive analysis CAMRAD II are presented, illustrating recent developments in the aerodynamics and dynamics models, and demonstrating the technology that is needed for an adequate calculation of rotorcraft behavior. Calculations of rotor performance, airloads, structural loads, and stability are presented, including comparisons with experimental data.

1. Nomenclature:

A	rotor disk area, πR^2
C_D	rotor equivalent drag, $C_p/\mu + C_X$
C_L	rotor lift force (wind axes), $L/\rho A(\Omega R)^2$
C_P	rotor power, $P/\rho A(\Omega R)^3$
C_T	rotor thrust, $T/\rho A(\Omega R)^2$
C_X	rotor drag force (wind axes), $X/\rho A(\Omega R)^2$
D/q	airframe drag divided by dynamic pressure
M	blade section Mach number
r	blade radial station
R	blade radius
c_n	blade section lift coefficient
c_m	blade section moment coefficient
α_s	shaft angle of attack (positive aft)
μ	advance ratio, (flight speed)/ ΩR
ρ	air density
σ	rotor solidity, (blade area)/A
Ω	rotor rotational speed

2. Introduction

CAMRAD II is an aeromechanical analysis of helicopters and rotorcraft that incorporates a combination of advanced technology, including multibody dynamics, nonlinear finite elements, and rotorcraft aerodynamics. For the design, testing, and evaluation of rotors and rotorcraft; at all stages, including research, conceptual design, detailed design, and development; it calculates performance, loads,

vibration, response, and stability; with a consistent, balanced, yet high level of technology in a single computer program; applicable to a wide range of problems, and a wide class of rotorcraft. Such capability is essential for helicopter problems, which are inherently complex and multidisciplinary.

A comprehensive helicopter analysis must calculate performance, loads, vibration, response, and stability. The multidisciplinary nature of helicopter problems means that similar models are required for all of these jobs. It follows that a comprehensive analysis must have a rotor wake model; account for drag and stall of the rotor blades; include nonlinear dynamics of the rotor and airframe; and model the entire aircraft. The analysis must perform trim, transient, and flutter tasks. The trim task finds the equilibrium solution (constant or periodic) for a steady state operating condition. The operating condition can be free flight (including level flight, steady climb or descent, and steady turns), or constrained (such as a rotor in a wind tunnel, with typically the thrust and flapping trimmed to target values). It is usually necessary to identify the control positions and aircraft orientation required to achieve the specified operating condition. The transient task numerically integrates the equations in time (from the trim solution), for a prescribed excitation. The flutter task obtains and analyzes differential equations for the system, linearized about trim (probably by numerical perturbation).

A modern comprehensive analysis must be able to analyze arbitrary configurations — whatever the designers can invent. The system configuration must be defined and changed by input to the analysis; it should not be necessary to change the code as long as the required physics are available. The definition of the solution procedure must be just as flexible as the definition of the configuration. The solution procedure must be defined and changed by input to the analysis; it should not be necessary to change the code as long as the required methods are available. CAMRAD II uses a building-block approach to achieve

.Presented at Heli Japan 98: AHS International Meeting on Advanced Rotorcraft Technology and Disaster Relief, April 21-23, 1998, Nagarafukumitsu, Gifu, Japan. Copyright © 1998 Wayne Johnson. All rights reserved.

flexibility in the model of the dynamic and aerodynamic configuration, and in the solution procedure. The mathematical model of the kinematics, dynamics, and response allows nonlinearities (structural, aerodynamic, and kinematics); and arbitrary large motion, including rigid body motions and large rotations of components relative to each other. Hence CAMRAD II can model the true geometry of a rotorcraft, including multiple load paths (such as a swashplate and control system, lag dampers, tension/torsion straps, and bearingless rotors); vibration control devices (such as pendulum absorbers or active control); arbitrary elastic axis and arbitrary hinge order; drooped and swept tips; and dissimilar blades. The building-block approach, separating the specification of the configuration, the aeromechanical model, and the solution procedure, is essential for expandability of the analysis. Otherwise the smallest change involves the entire analysis, and growth becomes increasingly harder as each new feature is added. The building-block approach also leads naturally to more general and more rigorous models. For ease of use, a shell is provided to build typical rotorcraft and rotor models, while the core input capability always gives complete flexibility to define and revise the model. The system pieces (building blocks) constitute the core analysis. The rotorcraft shell constructs the core input for an aircraft with one or two or more rotors; in free flight or in a wind tunnel; and an N-bladed rotor, with an articulated, hingeless, teetering, gimbaled, or bearingless hub; perhaps with a swashplate. The aerodynamic model includes a wake analysis to calculate the rotor nonuniform induced-velocities, using rigid, prescribed or free wake geometry. CAMRAD II is described in references 1 and 2.

This paper presents results from the comprehensive analysis CAMRAD II, illustrating recent developments in the aerodynamics and dynamics models. An important objective is to demonstrate the technology that is needed for an adequate calculation of rotorcraft behavior. Calculations of rotor performance, airloads, structural loads, and stability are presented, including comparisons with experimental data.

Comparisons with results from a flight test of the SA349/2 rotor show the influence of the rotor wake model at low speed. Comparisons with results from a flight test of a Puma helicopter having an experimental swept-tip rotor blade show the influence of the wake model at high speed, the influence of other features of the aerodynamic model, and the importance of an elastic blade analysis. A four-bladed articulated rotor with swept tips is considered to examine the influence of the wake model on rotor performance calculations. Comparisons with wind tunnel tests of an S-76 rotor show the capability to calculate rotor performance, and the importance of the blade structural-dynamic model. Calculations for a Lynx hingeless-rotor helicopter demonstrate the influence of the dynamic stall model on the calculated rotor power. Comparisons with results from a wind tunnel test of the MDART bearingless

rotor show the influence of the blade structural-dynamic model, and the rotor wake or dynamic inflow model.

3. SA349/2 Flight Test

A Gazelle SA349/2 helicopter with the an articulated hub and three research Grande Vitesse rotor blades was flight tested by Aerospatiale (ref. 3). The calculations included six-variable free flight trim; the standard forward flight wake model and free wake geometry; an elastic blade (nine harmonics, six blade modes); and flap-pitch-lag hinge sequence. Figure 1 shows the blade planform. Figure 2 shows the airloads measured for a low speed case, $C_T/\sigma = .065$ and $\mu = .14$, compared with calculations using various wake models. Figure 3 shows the calculated free wake geometry. The mutual interaction of the tip vortices produces a global rollup of the wake, analogous to the tip vortices forming behind a circular wing. The consequence of this global distortion is that the tip vortices are very close to the tip-path plane, actually passing over the blades on the sides of the disk. So the blade-vortex interaction is much stronger because of the self-induced distortion of the wake geometry. The measured airloads show significant blade-vortex interaction, which is not in the uniform inflow calculations at all (figure 2). Nonuniform inflow from a vortex wake model must be used. The free wake geometry is required to get sufficient magnitude of the calculated blade-vortex interaction on the blade tip. Generally, below an advance ratio of about $\mu = .20$, blade-vortex interaction is important, and therefore a free wake geometry calculation is needed to accurately obtain the separation between the wake and the rotor blades. The calculations were made using a tip vortex strength equal to the maximum bound circulation over the span of the blade, and a core radius of 20% chord. This core radius is larger than the true viscous core of a rotor tip vortex. The tip vortex strength is certainly smaller (the value used is the maximum possible), and there are probably other factors that require the core radius be increased to achieve good correlation with the measured blade-vortex interaction airloads. Figure 2 also suggests that on the retreating side the tip vortex strength is smaller than on the advancing side.

Figures 4 and 5 compare the measured and calculated blade structural loads. The mean values have been removed from both measured and calculated loads. The flight test data are obtained from measurements over one revolution, filtered to 10 harmonics. Pitch link loads were measured on all three blades. As with the airloads at this speed, nonuniform inflow has a significant effect on the calculated structural loads, and free wake geometry is required to adequately predict the loads. The airloads measurements show significant high frequency variations over six revolutions. So it is probably not appropriate (although tempting with results such as the flap bending moment in figure 4) to pay much attention to the high frequency details of the loads correlation. Figure 5 shows the pitch link loads, including calculations from the comprehensive analysis

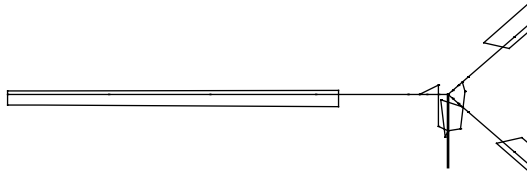


Figure 1. SA349/2 research Grande Vitesse rotor blade.

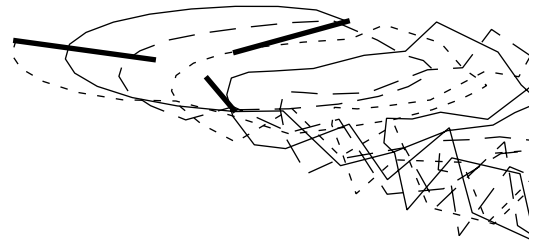


Figure 3. SA349/2 rotor at thrust $C_T/\sigma = .065$ and speed $\mu = .14$, calculated free wake geometry.

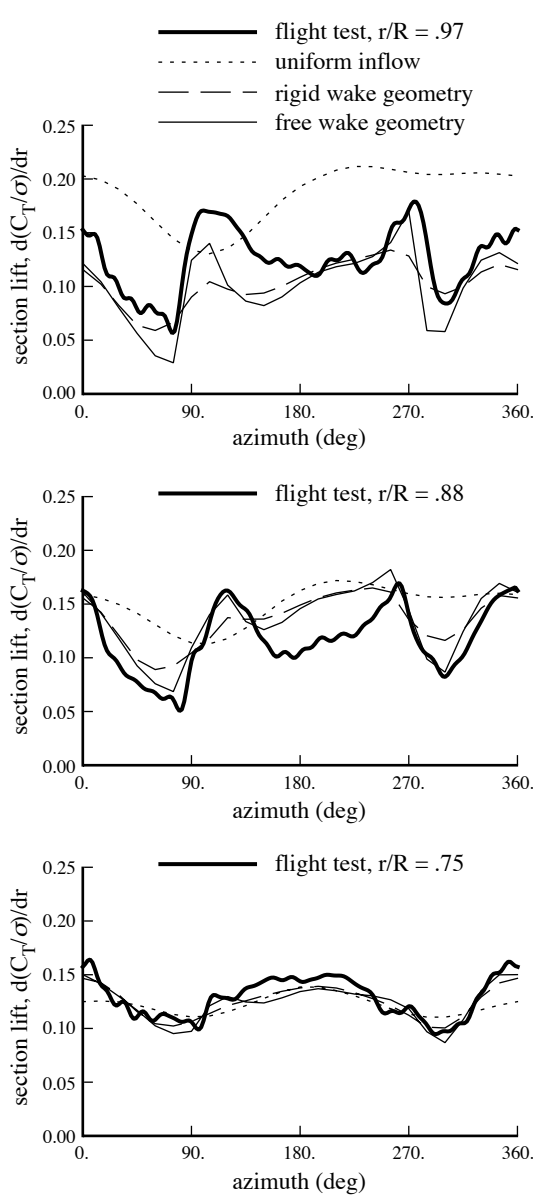


Figure 2. SA349/2 flight test at thrust $C_T/\sigma = .065$ and speed $\mu = .14$, blade section lift; influence of wake model.

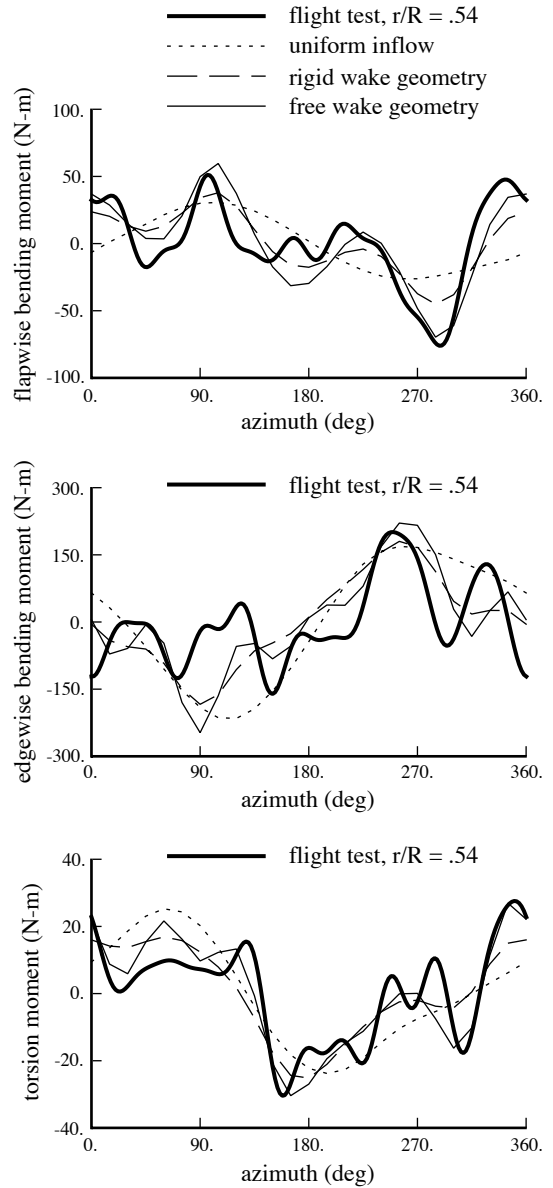


Figure 4. SA349/2 flight test at thrust $C_T/\sigma = .065$ and speed $\mu = .14$, blade bending and torsion moments (mean removed); influence of wake model.

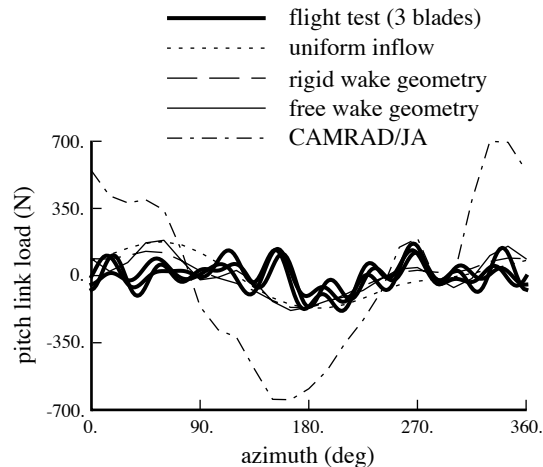


Figure 5. SA349/2 flight test at thrust $C_T/\sigma = .065$ and speed $\mu = .14$, pitch link loads (mean removed).

CAMRAD/JA, representing previous-generation technology. With CAMRAD/JA, the flexible control system is represented by a spring at the pitch bearing, and many second-order terms in the torsion dynamics are neglected. With CAMRAD II, the load path through the pitch link is being modelled, and the rigid body dynamics of all elements are handled without approximation. The approximations in CAMRAD/JA in this case lead to a large once-per-revolution pitch link load. The structural-dynamic models of CAMRAD II eliminate this error.

4. Puma Flight Test

A Puma helicopter with experimental swept-tip rotor blades was flight tested by the Royal Aeronautical Establishment at Bedford (ref. 4). The calculations were performed for an elastic rotor, trimming thrust and flapping with collective and cyclic pitch. The thrust, flapping, and shaft angle were obtained from the flight test data. Since the loading at high speed is negative on the advancing tip, the dual-peak wake model was used, with rigid wake geometry. Figure 6 shows the blade planform. Figure 7 shows the airloads measured at radial stations on the swept tip for a high speed case, $C_T/\sigma = .08$ and $\mu = .38$, compared with calculations using various wake models. Figure 8 shows the calculated free wake geometry. At this speed, the wake is swept downstream of the rotor disk before significant distortion occurs. The tip-path plane is tilted forward, so there is a component of the flight speed normal to the rotor disk that convects the vortices away from the blades. Hence blade-vortex interaction is much less important for this speed, and wake geometry and core size have less influence on the loading. The measured airloads do not exhibit as much blade-vortex interaction as at low speed, but still uniform inflow does not give good results (figure 7). Nonuniform inflow produces a significant change in the angle of attack over the rotor

disk, which is needed to calculate the airloads. The wake geometry distortion however has little effect. The correlation between measurement and calculation is good. Although this is a high advance ratio, the large sweep of the tip delays the formation of strong shocks. Strong shocks on the blade usually make it difficult to integrate the pressures chordwise to obtain the measured section lift.

Figure 9 compares the measured and calculated pitching moments on the blade sections. The correlation is fair at 92% radius, but worse outboard. The lifting-line wing model of CAMRAD II is second-order for lift, which contributes to the good correlation for lift; but it is still first-order for moments. The measured moments show a variation with radial station at the tip that is probably associated with three-dimensional aerodynamics. The angle of attack varies along the tip, but is small enough so at these Mach numbers (effectively reduced by the tip sweep) the static pitch moment is zero (the airfoil is symmetric). Thus the calculated pitching moment consists of the noncirculatory, unsteady airfoil term, which does not vary much with tip span station.

This case provides a good basis for examining the influence of various model features on the calculated behavior. Figure 10 compares second-order lifting-line theory (three-quarter chord collocation point) with first-order lifting-line theory (quarter chord collocation point). Second-order theory is needed to accurately handle large yaw and sweep, hence is important for this swept-tip blade at high speed. At low speed, first-order theory would overpredict the blade-vortex interaction. Second-order theory is also needed for low aspect-ratio blades. Figure 10 also compares the dual-peak and single-peak wake models. The dual-peak model handles the negative loading on the advancing blade tip. With the single-peak model, the tip vortex strength on the advancing side is obtained from the inboard, positive bound circulation peak in this case. The difference in lift on the advancing side reflects the different sign and strength of the tip vortex with the dual-peak and single-peak models.

Figure 11 shows the influence of the yawed flow and sweep aerodynamic corrections. The yawed flow corrections allow the use of two-dimensional airfoil table data for an infinite-aspect ratio wing in yawed flow, in particular producing a delay in stall, an increase in drag, and a spanwise drag force. The sweep aerodynamic correction here refers primarily to the use of the Mach number normal to the swept quarter chord line, which is important for highly-swept blade tips. The yawed flow effects are evident on the front and back of the rotor disk in figure 11, while the compressibility effects are evident on the advancing side. These corrections also have a substantial influence on the calculated rotor power.

This rotor at high speed has a large value of cyclic pitch, hence a large contribution from the unsteady aerodynamic loads. Figure 12 shows the influence of the unsteady aerodynamic model for attached flow on the section loads;

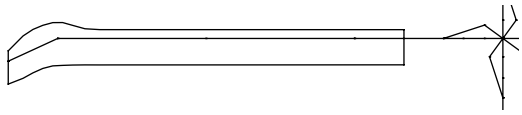


Figure 6. Puma experimental swept-tip rotor blade.

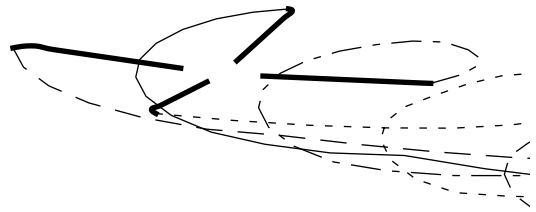


Figure 8. Puma rotor at thrust $C_T/\sigma = .08$ and speed $\mu = .38$, calculated free wake geometry.

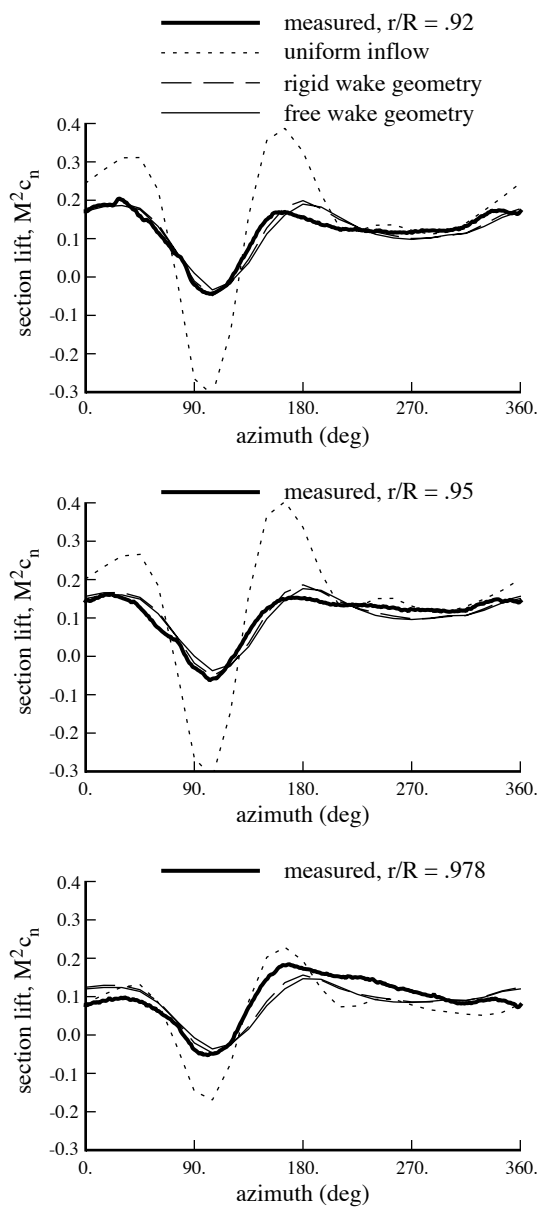


Figure 7. Puma flight test at thrust $C_T/\sigma = .08$ and speed $\mu = .38$, blade section lift; influence of wake model.

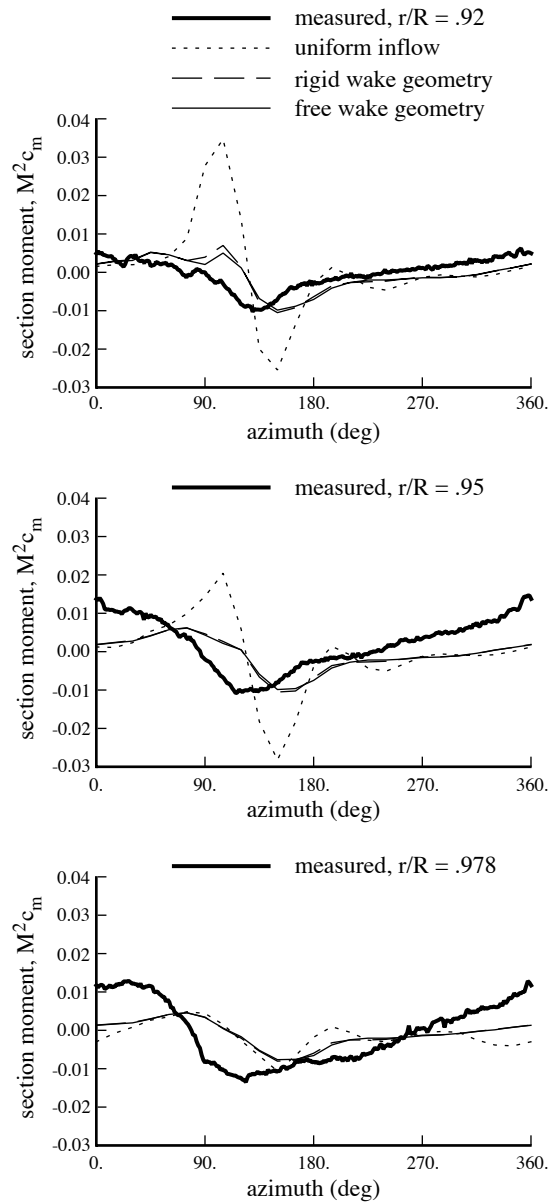


Figure 9. Puma flight test at thrust $C_T/\sigma = .08$ and speed $\mu = .38$, blade section moment; influence of wake model.

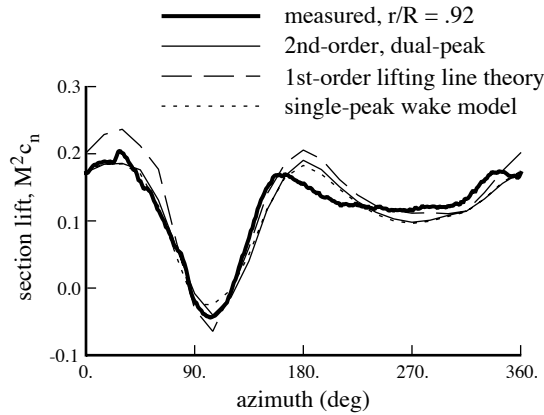


Figure 10. Puma flight test at thrust $C_T/\sigma = .08$ and speed $\mu = .38$, blade section lift; influence of aerodynamic model.

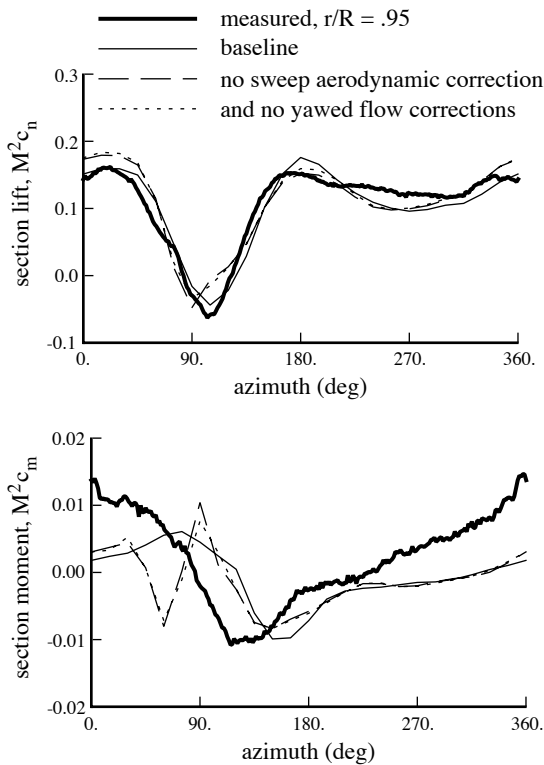


Figure 11. Puma flight test at thrust $C_T/\sigma = .08$ and speed $\mu = .38$, blade section lift and moment; influence of aerodynamic model.

both the total load and the unsteady term are plotted. The unsteady terms comprise a major part of the calculated loads for this case. All three models are based on thin-airfoil theory. The two-dimensional shed wake effects (the lift deficiency function) are accounted for in the vortex wake model.

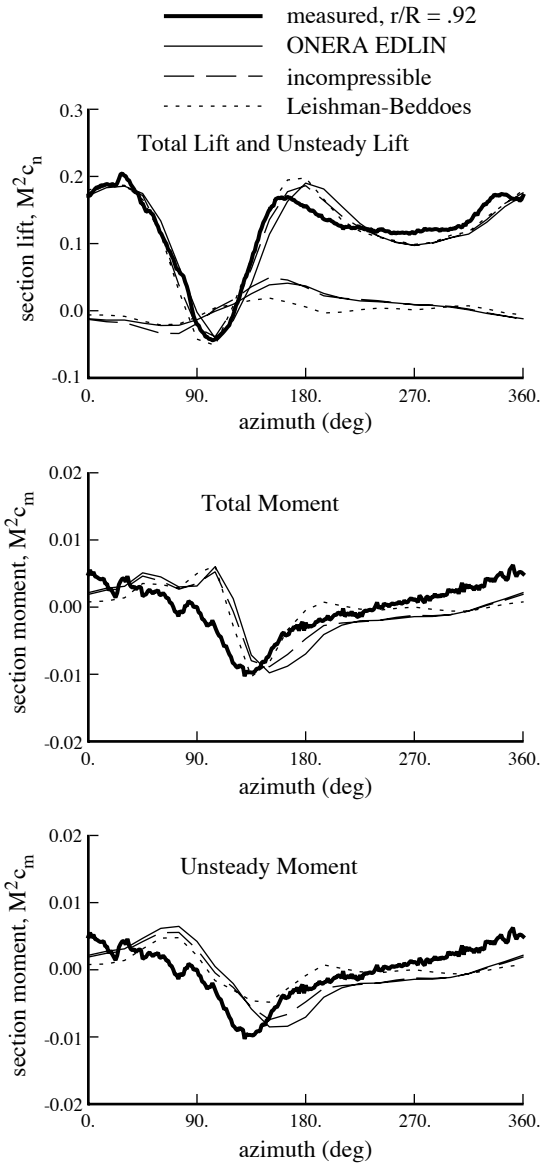


Figure 12. Puma flight test at thrust $C_T/\sigma = .08$ and speed $\mu = .38$, blade section lift and moment; influence of aerodynamic model.

Figure 13 show the influence of the blade structural-dynamic model on the calculated loads, comparing calculations that use elastic and rigid blades. The blade undergoes significant elastic twisting, so at least the blade torsion degrees of freedom are needed in the model. Elastic bending of the blade also has some influence, probably through coupling with the torsion motion. In this case the control system flexibility is adequately modelled by a spring at the pitch bearing; nearly the same results are obtained as with the complete swashplate and pitch link model. Figure 13 also shows the results obtained with no unsteady aerodynamics for attached flow. Without the

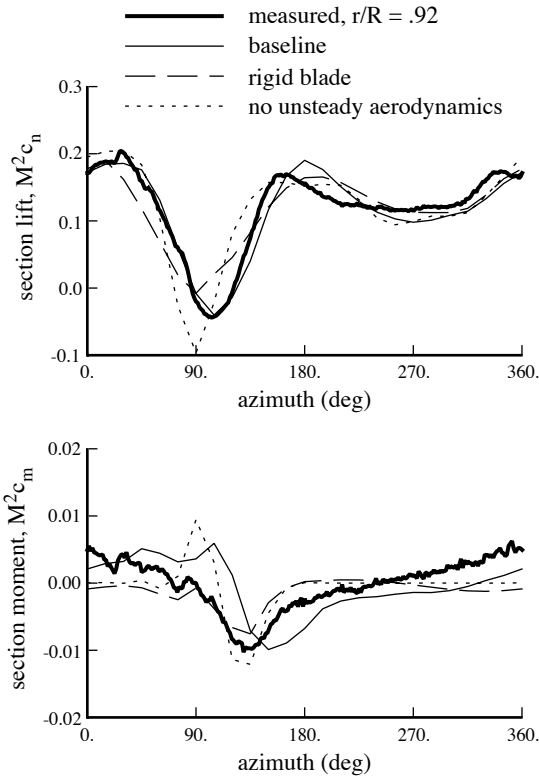


Figure 13. Puma flight test at thrust $C_T/\sigma = .08$ and speed $\mu = .38$, blade section lift and moment; influence of blade dynamic model.

unsteady terms, there is little torsion damping (the blade structural damping was increased to 3% in order to obtain a converged solution). The resulting change in the blade motion greatly affects the blade airloads.

5. Rotor Performance Calculations

To begin the examination of rotor performance calculations, consider a four-bladed articulated rotor with swept tips. Figure 14 shows the blade planform. The analysis used rigid blades, with just one harmonic of motion. The rotor was trimmed to zero flapping, with a thrust of $C_T/\sigma = .08$ and a propulsive force (airframe drag) of $D/qA = .0133$ (where A is the rotor disk area). Figure 15 shows the power calculated using uniform inflow, nonuniform inflow with rigid wake geometry, and nonuniform with free wake geometry. Figure 16 shows the induced power in terms of the ratio to ideal momentum theory power, and the profile power in terms of a mean blade drag coefficient.

For uniform inflow, the induced power factor (an input empirical constant) was set so the total power matched the nonuniform inflow calculation at high speed (figure 15). However, at high speed the distribution of power between induced and profile is quite different for uniform inflow and

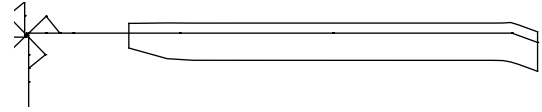


Figure 14. Swept-tip rotor blade for performance calculations.

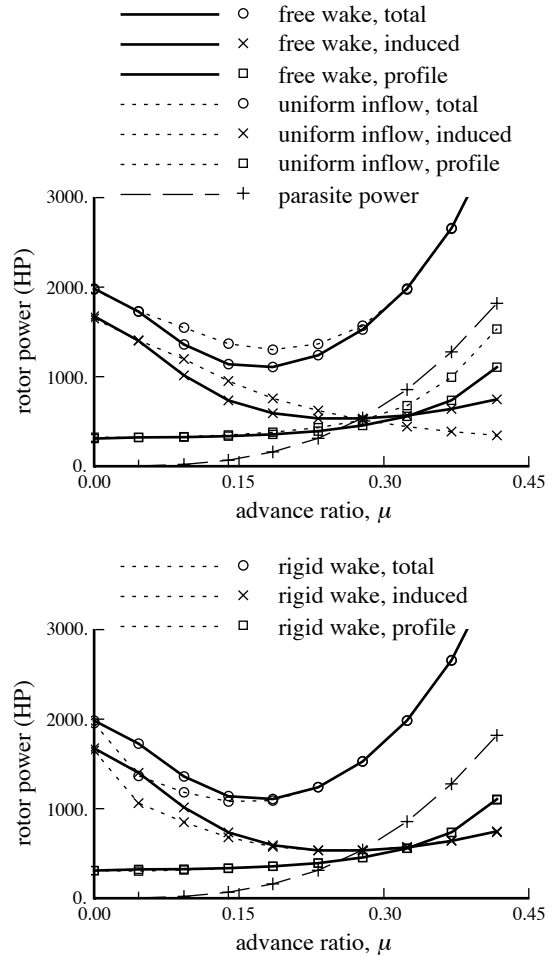


Figure 15. Performance calculations at thrust $C_T/\sigma = .08$ and propulsive force $D/qA = .0133$, rotor power; influence of wake model.

nonuniform inflow. Nonuniform inflow gives about twice the induced power, and correspondingly less profile power, than uniform inflow. The implications for rotor design are significant, since rotor parameters affect induced power and profile power differently. At low speed, the free wake model is needed to predict the power rise as speed decreases. Figure 16 shows the induced power factor reaching about 4.0 at high speed. This is a consequence of the loading distribution on a flapping rotor in forward flight. The retreating side of the disk can not have high loading

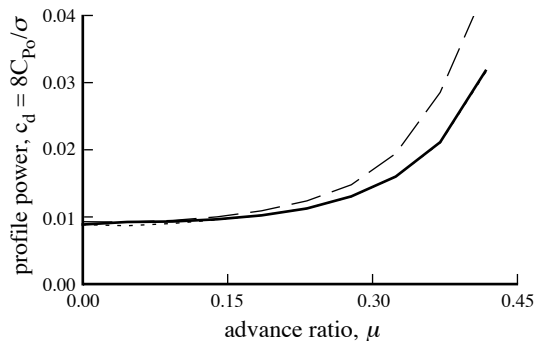
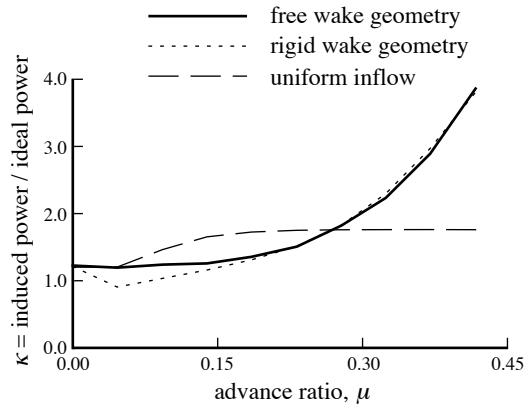


Figure 16. Performance calculations at thrust $C_T/\sigma = .08$ and propulsive $D/qA = .0133$, induced and profile power; influence of wake model.

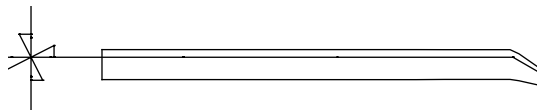


Figure 17. S-76 rotor blade.

because of the reduced velocity, and the advancing side must balance the retreating side. So the loading is concentrated on the front and rear, rather than uniformly distributed over the disk as required for ideal induced power. An induced power factor of 4.0 corresponds to an effective span of the lifting system equal to 50% of the rotor diameter.

6. S-76 Wind Tunnel Test

An S-76 main rotor was tested at high speed in the NASA Ames 40- by 80-Foot Wind Tunnel (ref. 5); at low speed in the NASA Ames 80- by 120-Foot Wind Tunnel (ref. 6); and in hover on a whirl tower at Sikorsky Aircraft (ref. 7). The blade has a swept and tapered tip. Figure 17 shows the blade planform. Figure 18 compares the calculated and measured hover performance. Figure 19 shows the calculated hover free wake geometry. In the absence of a

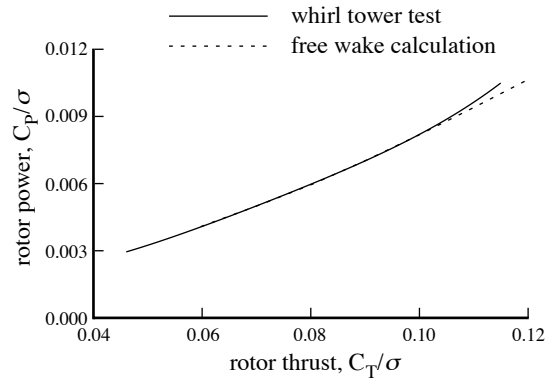


Figure 18. S-76 whirl tower test in hover, rotor power.

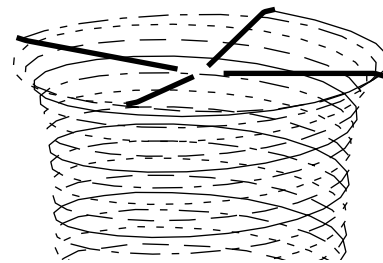


Figure 19. S-76 rotor in hover, calculated free wake geometry.

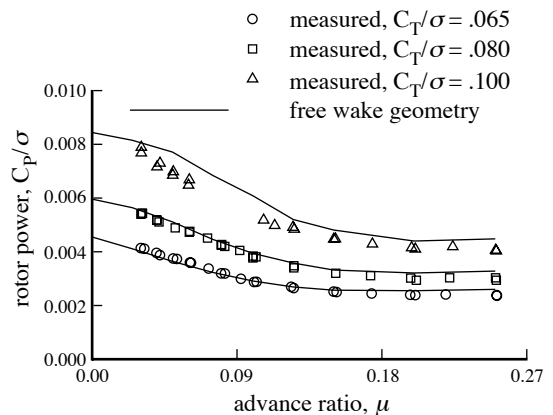


Figure 20. S-76 wind tunnel test, rotor power.

calculation of the detailed flow field near the hovering blade tip, the initial convection velocities at the tip vortices are defined such that the wake leaves the wing tangent to the wing surface. Progress in the analysis of hovering rotors is measured by a narrowing focus of empiricism: from a factor on the uniform induced velocity for momentum theory; to parameters defining the wake geometry for prescribed methods; to the initial formation, wake extent, and core size for free wake methods based on inviscid aerodynamics.

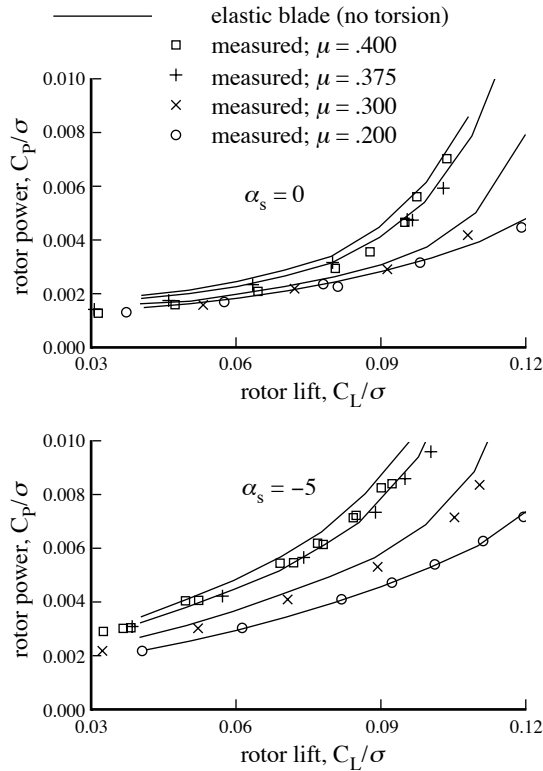


Figure 21. S-76 wind tunnel test, rotor power.

Figure 20 compares the calculated performance with low speed wind tunnel measurements, for three rotor thrust levels. The calculations used wake parameters developed for low speed, with six revolutions of the wake. The overprediction of the power at high thrust is relatively independent of speed, suggesting that the drag increase with lift in the airfoil tables might be too great.

Figure 21 compares the calculated performance with high speed wind tunnel measurements, for two rotor shaft angles and four speeds. The correlation is good. The analysis used an elastic blade model, but with the blade torsion motion suppressed. Both the measured and the calculated results include wind tunnel wall corrections. The wall correction has the classical form, giving a rotor angle of attack increase $\Delta\alpha$ that is proportional to the rotor lift divided by dynamic pressure, L/q . Thus in the measured data the wind tunnel balance forces are resolved into rotor lift and drag assuming that the wind axes are tilted forward by the angle $\Delta\alpha$. The calculations are performed for a shaft angle of attack $\alpha_s + \Delta\alpha$ relative the wind tunnel velocity, hence tilted aft from the geometric shaft angle of attack. Figures 22 and 23 show the rotor power and drag force (negative propulsive force) at these operating conditions, for three analytical models: rigid blade, elastic blade without torsion, and elastic blade. At low speed there is little influence of the blade elastic motion, so all three models give comparable results, and correlate well with the

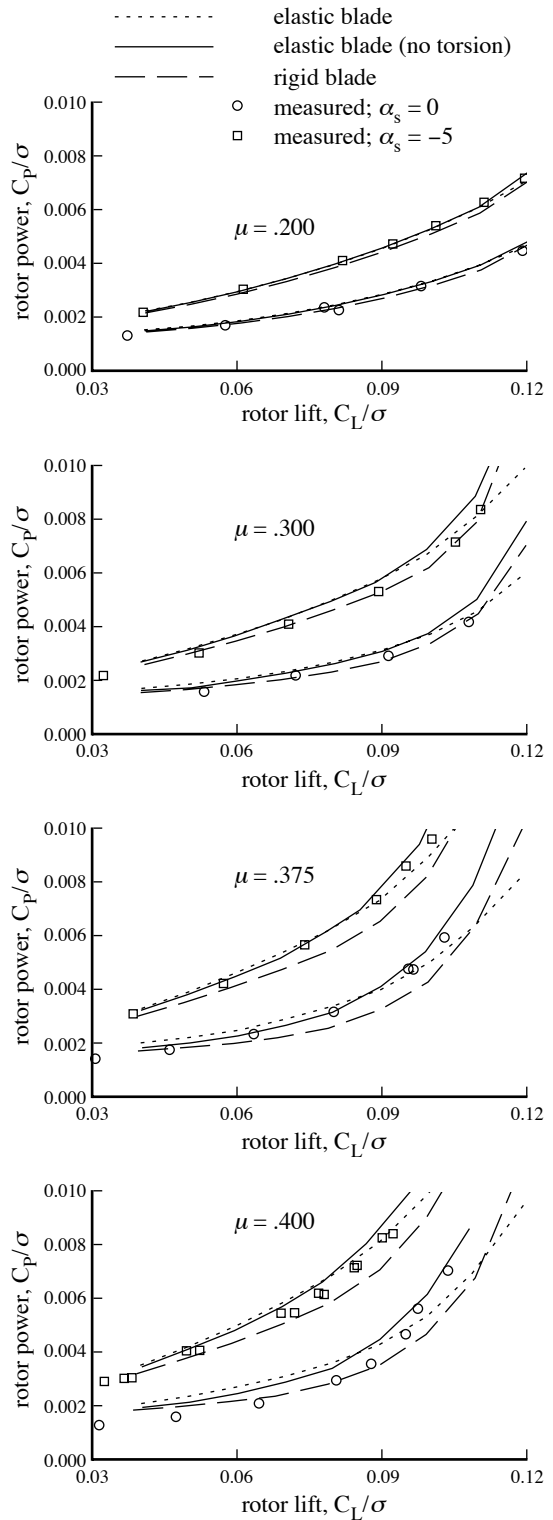


Figure 22. S-76 wind tunnel test, rotor power; influence of blade dynamic model.

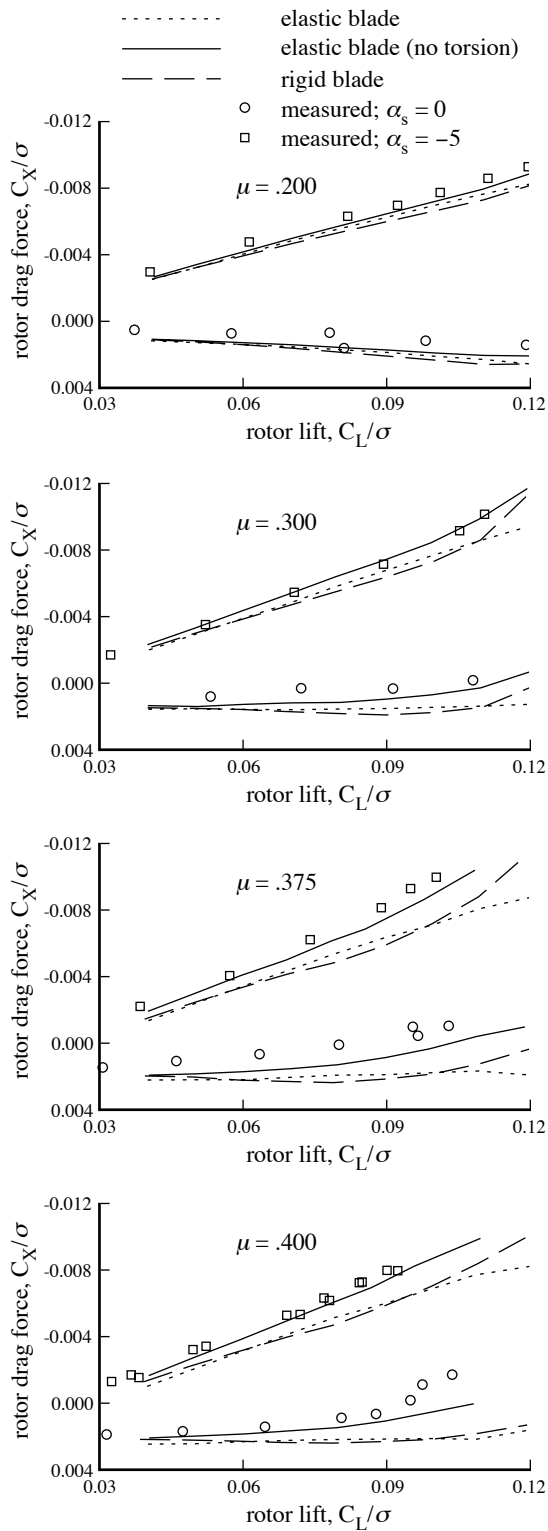


Figure 23. S-76 wind tunnel test, rotor drag force; influence of blade dynamic model.

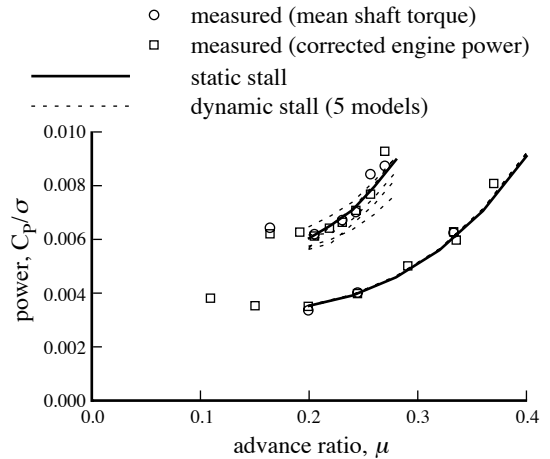


Figure 24. Lynx flight test at weight $C_T/\sigma = .07$ and $.11$, rotor power (no blade lag or torsion motion).

measurements. At high speed, the calculations for an elastic blade without torsion motion compare well with both measured power and measured propulsive force. For a rigid blade, the power and propulsive force are underpredicted. For an elastic blade, including the torsion motion, the propulsive force is underpredicted. The total power consists of profile, induced, and parasite terms, the parasite power being determined by the propulsive force. So if the propulsive force is not accurately calculated, matching the measured total power simply means that there must be errors in the profile or induced power calculation, which can not be considered good correlation. It is not concluded that this rotor is very stiff in torsion, but rather that the calculations using the available input data exhibit too much torsion motion. For further progress, a re-examination of the structural-dynamic input data is required, including the control system stiffness.

7. Lynx Flight Test

A Lynx hingeless-rotor helicopter was flight tested by Westland Helicopters up to and beyond the stall boundary (ref. 8). The flight test included speed sweeps at low and high gross weight, extending into regimes with significant dynamic stall. Figure 24 compares the measured power with calculations using several dynamic stall models. This figure is just a reality check rather than correlation, since the calculations were performed without elastic lag or torsion motion of the blades (to isolate the effects of the different aerodynamic models), and because the static airfoil data were not measured much beyond the onset of stall. At normal operating conditions, dynamic stall can be neglected. At high lift or high speed however, even the rotor power depends on the dynamic stall behavior of the blades. Figure 25 shows the influence of the aerodynamic model on the calculated rotor equivalent drag as a function of rotor lift (the rotor equivalent drag measures just the induced and profile power). Calculations are presented

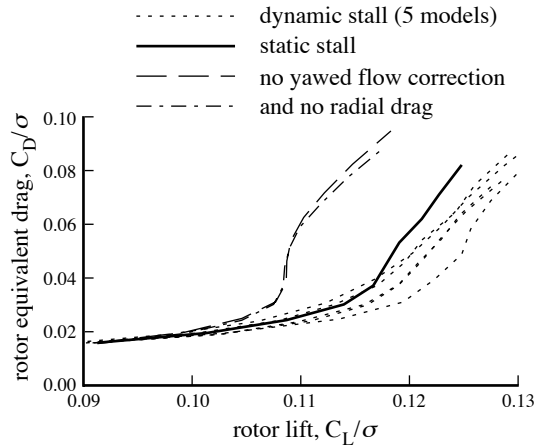


Figure 25. Lynx rotor at advance ratio $\mu = .25$ and shaft angle of attack -4 deg, calculated rotor drag (no blade lag or torsion motion); influence of aerodynamic model.

using several dynamic stall models, as well as with and without yawed flow corrections. This is not a new result (see ref. 9), except for the presence of five dynamic stall models instead of just one. But figure 25 captures the state-of-the-art well: the effects of yawed flow and dynamic stall are extremely important in rotor performance, yet their calculation in practical analyses must rely on empirical models.

8. MDART Wind Tunnel Test

The McDonnell Douglas Advanced Bearingless Rotor (MDART) was tested in the NASA Ames 40- by 80-Foot Wind Tunnel (refs. 10 and 11). This rotor was a reproduction version of the MD900 rotor. Figure 26 shows the blade planform. Four CAMRAD II models were developed. The "early" model is based on information available at the time of the wind tunnel test and during subsequent correlation work (refs. 10 and 11). The "updated" model has changes in the blade distributed properties (structural, inertial, and aerodynamic), developed based on correlation of other analyses with nonrotating blade shake test data. For the CAMRAD II input, the snubber stiffness and damping were adjusted to match the lag frequency and damping at nominal thrust in hover (the actual properties of the nonlinear elastomeric snubber were not known in detail). The basic early and updated models have a flexbeam consisting of a single load path. The blade was represented by four beam elements (one for the swept tip); the pitch case by one element; and the flexbeam by four elements (the first and last rigid). Using more elements did not change the results significantly. The MD900 flexbeam is actually attached to the hub through two legs inboard of 8.3% radius. Therefore a two-leg flexbeam model was also constructed (figure 26), using the CAMRAD II core input capability to revise the one-leg model constructed by the rotorcraft shell. Estimates of the

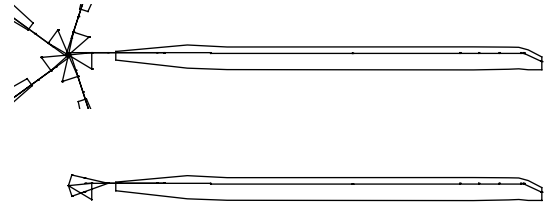


Figure 26. MDART rotor blade (1-leg and 2-leg flexbeam models).

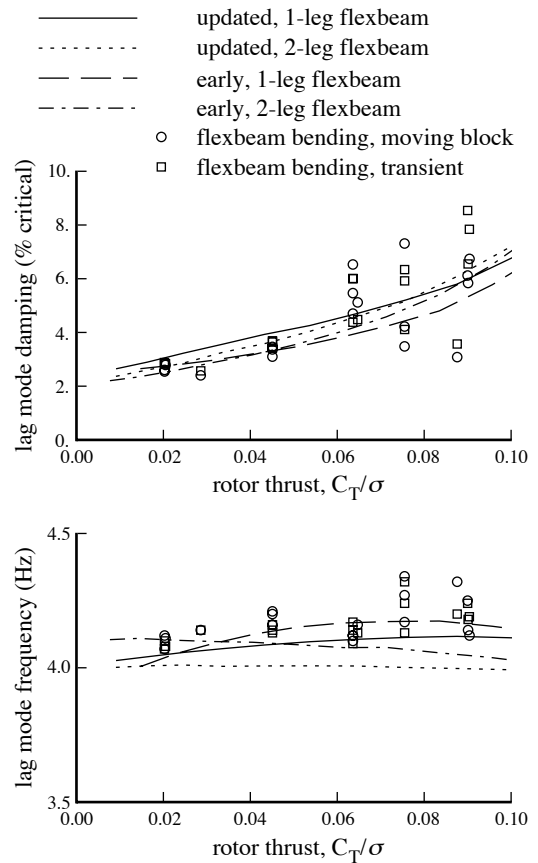


Figure 27. MDART wind tunnel test in hover; measured and calculated blade lag mode stability.

structural and inertial properties of the two legs were used. The blade loads were calculated in the same manner as they were measured: the results shown are the load minus the zero point load (nonrotating with blades on the flapping stop); weight tares are not included here, in either the measurements or the calculations.

Figures 27 and 28 compare the measured and calculated blade stability, for the four models of the rotor. The calculated trends with thrust and speed are correct. Note that for the speed sweep, the shaft angle varies with speed until

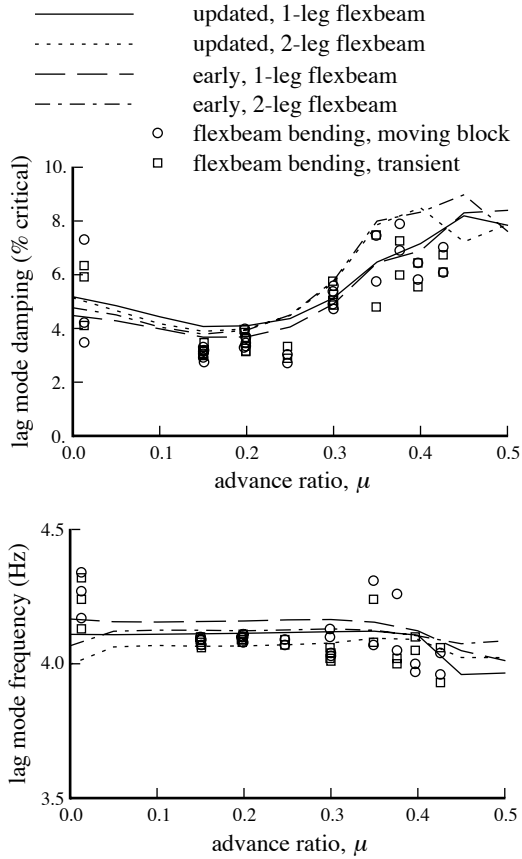


Figure 28. MDART wind tunnel test in forward flight, at thrust $C_T/\sigma = .075$; measured and calculated blade lag mode stability.

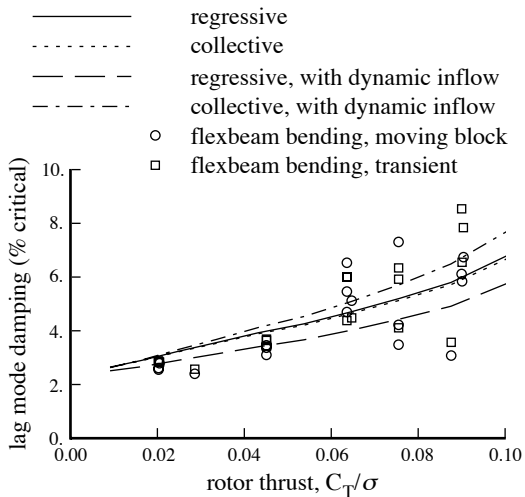


Figure 29. MDART wind tunnel test in hover; influence of dynamic inflow on calculated blade lag mode stability (updated model with 1-leg flexbeam).

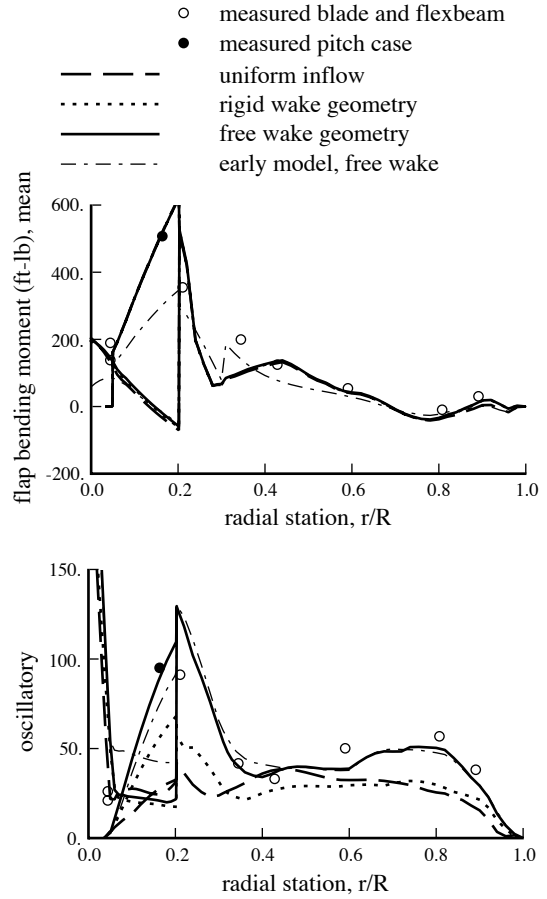


Figure 30. MDART wind tunnel test, at advance ratio $\mu = .20$ and thrust $C_T/\sigma = .074$; flap bending moment.

an advance ratio of $\mu = .4$, and then is fixed at -10 deg to match the test conditions. The four models produce similar results for the damping, which gives confidence in results obtained early in the rotor development process for such a bearingless rotor configuration. Figure 29 shows the influence of dynamic inflow on the calculated lag mode stability (for the updated, 1-leg flexbeam model). Dynamic inflow has a moderate influence in hover, decreasing lag damping; its influence decreases with forward speed.

Figures 30 and 31 compare the measured and calculated bending moments in forward flight. The calculated mean flap loads are good with the updated model (figure 30); the early model underpredicts the pitch case load. The variations in the calculated load near 30% radius are caused by the values used for the twist of the structural principal axes. The free wake geometry is needed for good results at the tip in hover. At advance ratio $\mu = .20$, the calculated oscillatory flap loads are good with the updated model and free wake geometry. At advance ratio $\mu = .37$ (not shown), the calculated oscillatory flap loads are low on the pitch case and the blade tip. The calculated mean lag loads are good with the updated model, except at 60% radius (figure

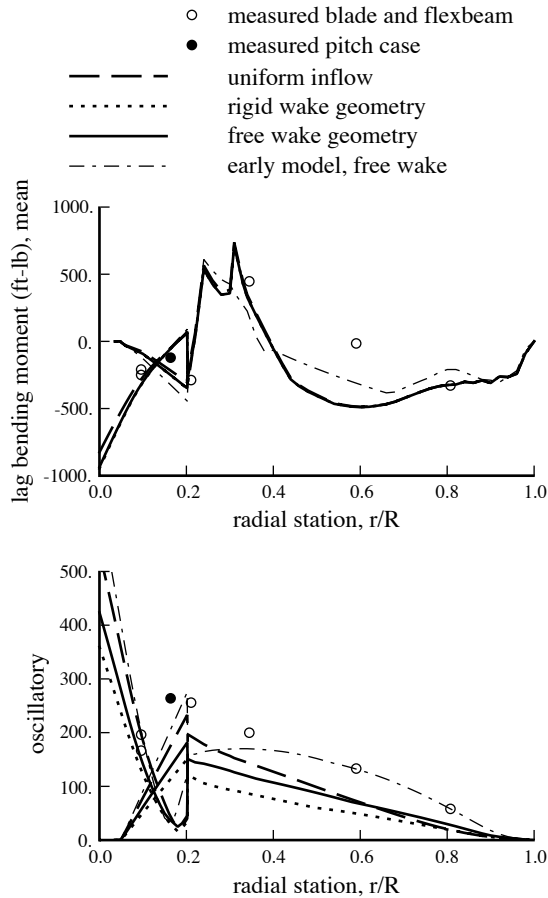


Figure 31. MDART wind tunnel test, at advance ratio $\mu = .20$ and thrust $C_T/\sigma = .074$; lag bending moment.

31). This discrepancy might be a result of the values used for the chordwise offset of the tension center. The calculated oscillatory loads are low.

Figures 32 and 33 show the influence of hub moment trim on the oscillatory bending loads at .37 advance ratio. In the calculations, the rotor is trimmed to zero flapping (as in figures 30 and 31) or trimmed to the measured hub moment. While the test was generally conducted with the rotor trimmed to small flapping (flapping being derived from a flexbeam bending moment measurement), this test point had significant hub moments. Hence trimming to the measured hub moment improves the calculated oscillatory loads substantially, while the calculated mean loads were unaffected. Figures 32 and 33 also show the loads calculated using the 2-leg flexbeam model. There are differences between the results of the 1-leg and 2-leg models, but probably refining the structural dynamic properties of the 1-leg model would be most productive in improving the calculations.

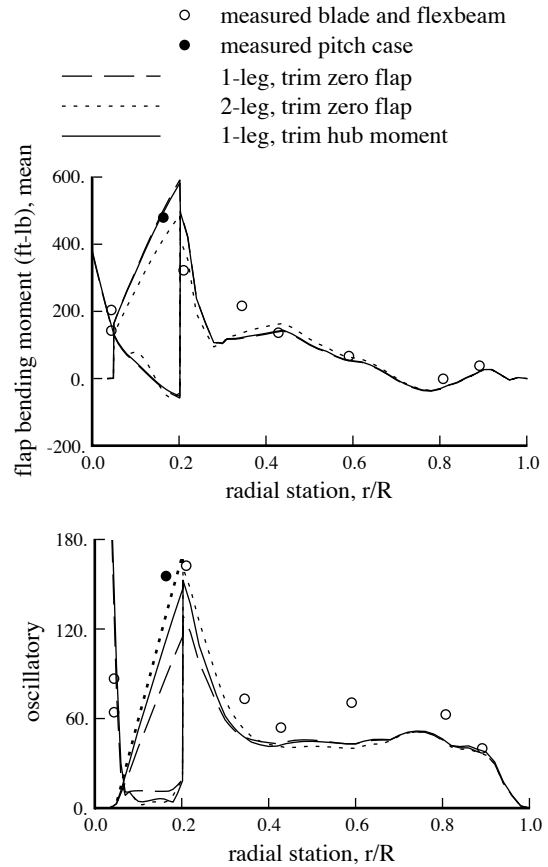


Figure 32. MDART wind tunnel test, at advance ratio $\mu = .37$ and thrust $C_T/\sigma = .075$; flap bending moment (updated model, rigid wake geometry).

9. Concluding Remarks

An objective of this paper is to demonstrate the technology that is needed for an adequate calculation of rotorcraft behavior, by showing comparisons of the CAMRAD II calculations with experimental data. A good wake model is required for most problems: nonuniform inflow from a vortex wake model for loads and performance, and at least a dynamic inflow model for stability. Below an advance ratio of about $\mu = .20$ or $.25$, a free wake geometry calculation is required as well. The aerodynamic model must include second-order lifting-line theory; a dual-peak wake model at high speed; yawed flow and sweep aerodynamic corrections; unsteady aerodynamics for attached flow; and dynamic stall. The structural-dynamic model influences not only stability and loads calculations, but airloads and performance as well.

Of course, all available technology is not needed in all cases. For example, a free wake geometry calculation is not usually needed at high advance ratio. A dynamic stall model is not needed in normal operating conditions. Sometimes a rigid blade model is quite sufficient.

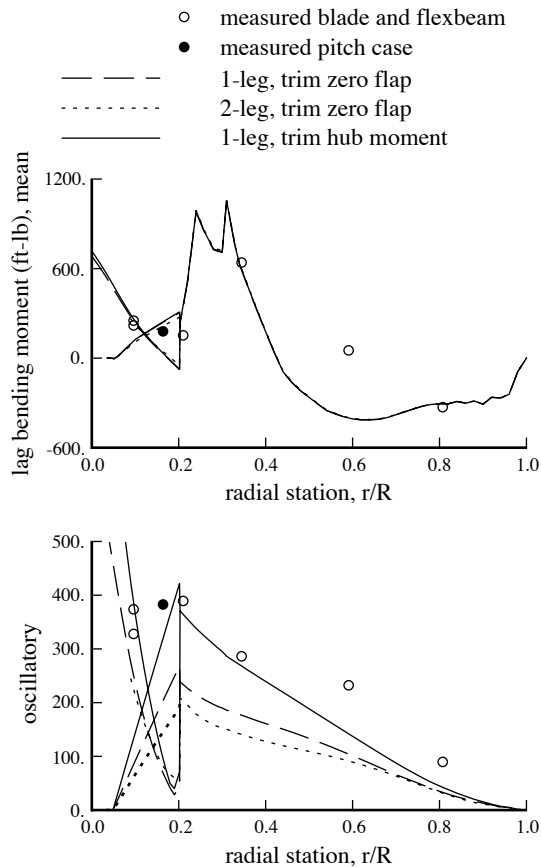


Figure 33. MDART wind tunnel test, at advance ratio $\mu = .37$ and thrust $C_T/\sigma = .075$; lag bending moment (updated model, rigid wake geometry).

There are some features of available technology that probably are not needed. A wake model constructed using line segments is adequate. The use of sheet panels does not improve, or often even change, the aerodynamic calculations. With a reasonable number of elements representing the rotor blade, any large deflection effects are captured by the rigid body motion (always exact in CAMRAD II), and a second-order model of the beam element elastic motion is adequate. Even in cases of extremely large bending amplitude, the exact expressions for extension and torsion produced by bending (which require significant computation time to evaluate by numerical integration) need not be used.

In general, it must be concluded that the technology needed is all that is available — and more. The good correlation between calculations and measurements that can be achieved does not mean that everything is known about the aeromechanics of rotors. The examples presented in this paper focus attention on a number of issues, particularly the following.

Developing the input data for a comprehensive analysis model is very large job. The S-76 and MDART correlation efforts illustrate how most projects would benefit from a refinement of the input data, including checks with subsystem tests. The discrepancies in correlation are probably not entirely attributable to the input information however. Better structural-dynamic models must be developed. Structural models are needed for those parts of blades and flexbeams that are not beamlike, as at constraints, junctions, and changes in properties. At least it is desirable to be able to define equivalent section properties for a beam model in such cases.

The effects of yawed flow and dynamic stall are extremely important in rotor performance, yet their calculation in practical analyses must rely on empirical models. The interaction between wake and blades in forward flight is governed by the strength and core size of the tip vortices, but these characteristics are obtained using modelling assumptions from the bound circulation distribution and input parameters. In the absence of a calculation of the detailed flow field near the hovering blade tip, the initial convection velocities at the tip vortices are defined such that the wake leaves the wing tangent to the wing surface. A Navier-Stokes analysis of tip vortex formation and its interaction with the following blades would be most useful.

10. References

- 1) Johnson, W. "CAMRAD II, Comprehensive Analytical Model of Rotorcraft Aerodynamics and Dynamics." Johnson Aeronautics, Palo Alto, California, 1992-1997.
- 2) Johnson, W. "Technology Drivers in the Development of CAMRAD II." American Helicopter Society, Aeromechanics Specialists meeting, San Francisco, January 1994.
- 3) Yamauchi, G.K.; Heffernan, R.M.; and Gaubert, M. "Correlation of SA349/2 Helicopter Flight Test Data with a Comprehensive Rotorcraft Model." European Rotorcraft Forum, Germany, September 1986; Journal of the American Helicopter Society, Volume 33, Number 2, April 1988.
- 4) Bousman, W.G.; Young, C.; Gilbert, N.; Toulmay, F.; Johnson, W.; and Riley, M.J. "Correlation of Puma Airloads — Lifting-Line and Wake Calculation." NASA TM 102212, November 1989.
- 5) Johnson, W. "Performance and Loads Data from a Wind Tunnel Test of a Full-Scale Rotor with Four Blade Tip Planforms." NASA TM 81229, September 1980.
- 6) Shinoda, P.M. "Full-Scale S-76 Rotor Performance and Loads at Low Speeds in the NASA Ames 80- by 120-Foot Wind Tunnel." NASA TM 110379, April 1996.
- 7) Jepson, D.; Moffitt, R.; Hilzinger, K.; and Bissell, J. "Analysis and Correlation of Test Data From an Advanced Technology Rotor System." NASA CR 3714, August 1983.
- 8) Lau, B.H.; Louie, A.W.; Sotiriou, C.P.; and Griffiths, N. "Correlation of the Lynx-XZ170 Flight-Test Results Up To and Beyond the Stall Boundary." American Helicopter Society Forum, May 1993.
- 9) Harris, F.D.; Tarzanin, F.J., Jr.; and Fisher, R.K., Jr. "Rotor High Speed Performance, Theory vs. Test." Journal of the American Helicopter Society, Volume 15, Number 3, July 1970.
- 10) Nguyen, K.; McNulty, M.; Anand, V.; and Lauzon, D. "Aeroelastic Stability of the McDonnell Douglas Advanced Bearingless Rotor." American Helicopter Society Forum, May 1993.
- 11) Nguyen, K.; Lauzon, D.; and Anand, V. "Computation of Loads on the McDonnell Douglas Advanced Bearingless Rotor." American Helicopter Society Forum, May 1994.